Enhanced activity for the oxygen reduction reaction in microporous water

Agnes Thorarinsdottir, Daniel Erdosy, Cyrille Costentin, Jarad Mason, Daniel Nocera

To cite this version:

Agnes Thorarinsdottir, Daniel Erdosy, Cyrille Costentin, Jarad Mason, Daniel Nocera. Enhanced activity for the oxygen reduction reaction in microporous water. Nature Catalysis, 2023, 6 (5), pp.425-434. 10.1038/s41929-023-00958-9 . hal-04682507

HAL Id: hal-04682507

https://hal.science/hal-04682507v1

Submitted on 30 Aug 2024

Enhanced activity for the oxygen reduction reaction in microporous water

Authors:

Agnes E. Thorarinsdottir[1,†], Daniel P. Erdosy[1,†], Cyrille Costentin[2,3,*], Jarad A. Mason[1,*], and Daniel G. Nocera[1,*]

Affiliations:

[1] Department of Chemistry and Chemical Biology, Harvard University, Cambridge, Massachusetts 02138, United States.

[2] Département de Chimie Moléculaire, CNRS, Université Grenoble Alpes, Grenoble 38000, France.

[3] Université de Paris, Paris 75013, France.

[†] These authors contributed equally to this work.

Corresponding author email:

cyrille.costentin@univ-grenoble-alpes.fr (C.C.); mason@chemistry.harvard.edu (J.A.M.);
dnocera@fas.harvard.edu (D.G.N.)

Abstract: Electrocatalysis of small gas molecules driven by renewable energy sources offers a promising route to carbon-neutral fuels and chemicals. Such small molecule conversion reactions rely on water as a source of protons and electrons, however, thus limiting energy and power densities owing to the low solubility of gas molecules in water. The oxygen reduction reaction (ORR) is an exemplar of such limitations. Here, we demonstrate that the high O_2-carrying capacity of microporous water enhances ORR electrocatalysis in water. Use of silicalite-1 nanocrystals to form an O_2-concentrating microporous electrolyte solution increases the ORR current so much so that the activity of Pt, typically thought to be an ideal ORR catalyst, is partially limiting, thus allowing the intrinsic catalytic ORR activity of Pt to be measured directly.

Catalysis of small gas molecules driven by electricity generated from renewable energy sources offers a promising route to carbon-neutral fuels and chemicals[1–4]. Large-scale implementation of small molecule conversions relies on water as a source of protons and electrons[5–7]. The exemplar energy conversion process involving gases is the $H_2/O_2 \leftrightarrow H_2O$ fuels cycle[5] where renewable energy may be stored in the chemical bonds of the products of the water-splitting reaction, O_2 and H_2, and then recovered on demand with the oxygen reduction reaction (ORR), via a hydrogen fuel cell[8]. The low solubilities of O_2 and H_2 in water[9], and more generally of most other small gas molecules of energy consequence (e.g., N_2, CO_2), significantly limits the achievable current densities using liquid-phase electrocatalysis. Whereas gas- or vapor-fed gas diffusion electrodes enable one-to-two orders of magnitude greater current densities[10–13], key challenges remain because of the complexity of the two-phase and three-phase interfaces, complex and non-uniform catalyst microenvironments, and electrode flooding, which adversely affect their durability and long-term performance[14–16]. Moreover, the requirements of certain device configurations, such as those of various membrane reactors[17–19], preclude the possibility of a gas–liquid interface. This provides an imperative to overcome mass transport limitations imposed by poor gas solubilities. One strategy to circumvent the low solubility of gases in water focuses on the introduction of organic additives such as perfluorocarbons. The resulting two-phase aqueous–organic systems provide higher gas solubilities owing to the much higher solubilities of non-polar gases in organic media as compared to aqueous media[20]. Nevertheless, high perfluorocarbon concentrations of 25 vol % are necessary to achieve even a modest increase of 1.8× in ORR current in alkaline conditions[21]. An alternative strategy centers on employing porous solids that remain empty and able to adsorb gas molecules even when uniformly dispersed in a solvent, so-called porous liquids[22–25]. Though most porous liquids contain organic solvents, certain microporous nanocrystals with hydrophobic internal surfaces and hydrophilic external surfaces can form aqueous porous liquids—termed "microporous water"—that feature much higher gas concentrations than conventional aqueous solutions[26]. The weak physisorptive interactions that lead to the high gas capacities of microporous water also facilitate fast gas exchange kinetics, making these solutions well-suited for liquid-phase electrochemical catalysis. The approach of boosting gas concentration through physisorptive interactions provides a path to catalysis at higher operating currents and also could enable the assessment of the intrinsic activity of electrocatalysts over a wide potential range, as mass transport limitations imposed by the diffusion of gaseous substrates to the catalyst surface would be minimized or completely circumvented.

We report herein the ORR activity of a Pt/C electrocatalyst in water endowed with microporosity

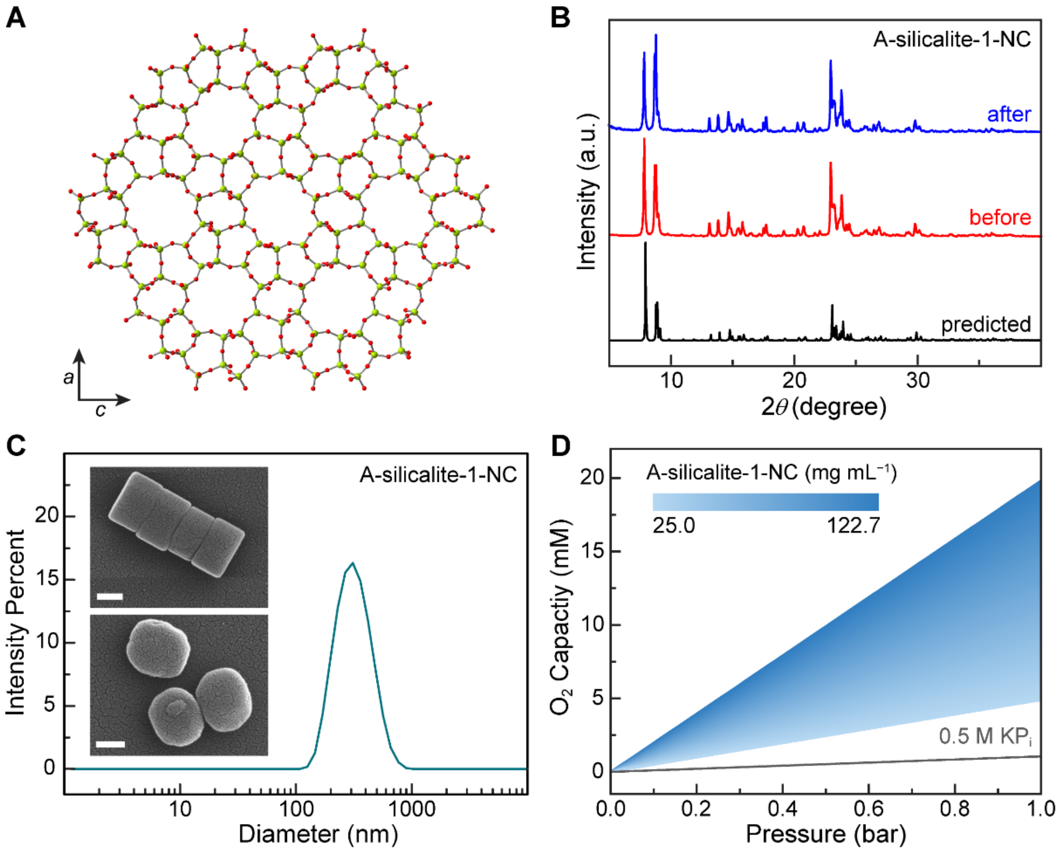

Fig. 1 | Characterization of A-silicalite-1-NCs in solid state and aqueous solution. (**A**) Part of a crystal structure of silicalite-1-NC viewed along the crystallographic *b* axis; yellow green and red spheres denote Si and O atoms, respectively. (**B**) PXRD data collected for A-silicalite-1-NCs before (red) and after (blue) performing ORR catalysis in phosphate-buffered water (0.5 M in phosphorus) solutions at pH 7.0. Predicted powder pattern derived from the reported crystal structure is shown in black for comparison. (**C**) DLS particle size distribution of A-silicalite-1-NCs in phosphate-buffered water (0.5 M in phosphorus) solution at pH 7.0. *Inset*: SEM images of A-silicalite-1-NCs before ORR catalysis as viewed top-down (lower) and side-on (upper); white scale bars denote 100 nm. (**D**) Comparison of O_2 capacities of phosphate-buffered water (0.5 M in phosphorus) solutions at pH 7.0 without (grey) and with 25.0–122.7 mg mL^{-1} of A-silicalite-1-NCs (blue).

afforded by the hydrophobic cavities of zeolitic nanocrystals (silicalite-1-NCs). Aqueous dispersions of silicalite-1-NCs absorb and release O_2 reversibly, storing up to two orders of magnitude more O_2 than pure water[26]. In the presence of a 6.7 volume % aqueous solution of these O_2-concentrating nanocrystals, a 3.8–3.9× increase in the ORR current density is observed for a Pt/C electrocatalyst in acidic and neutral conditions. This increase in current density is such that Pt, typically considered to be a superior ORR catalyst[27], becomes the partial rate limiting determinant of ORR in the microporous water, thus suppressing the mass transport contribution and allowing the intrinsic catalytic ORR activity of Pt to be easily measured by rotating disk electrode voltammetry.

Results

Solid- and solution-state characterization of silicalite-1-NCs. Silicalite-1 is a pure silica zeolite with hydrophobic micropores[28] that displays an MFI structure-type[29] with two types of interconnected channels: sinusoidal and straight channels running along the crystallographic *a* and *b* axis (Fig. 1A), respectively. Silicalite-1-NCs were synthesized by a hydrothermal route using a modification of a reported procedure[30] (A-silicalite-1-NCs; Methods Section, Material synthesis). The crystallinity and phase purity of A-silicalite-1-NCs were verified by powder X-ray diffraction (PXRD) (Fig. 1B) and the morphology was assessed by scanning electron microscopy (SEM). The A-silicalite-1-NCs exhibit a cylindrical morphology (Fig. 1C, inset and Supplementary Fig. 1), as indicated by disc-shaped (average diameter of 197 ± 16 nm; Supplementary Fig. 2 and Supplementary Table 1) and rectangular (height ca. 125 nm) features when viewed from top-down and side-on, respectively. Gas adsorption measurements provided an O_2 adsorption capacity of $3.8(4) \times 10^2$ mM bar^{-1} at 20 °C for the solid-state material (Supplementary Table 2), which is far higher than the 1.42 mM bar^{-1} of O_2 that is dissolved in water at the same temperature (Fig. 1D, grey trace). Owing to their hydrophilic external surfaces that are capped with silanol and silanolate species, A-silicalite-1-NCs may be dispersed in a variety of neutral aqueous solutions (Supplementary Fig. 3), including high-concentration phosphate buffers (Fig. 1C). Although aggregation of A-silicalite-1-NCs does occur over time in aqueous solutions at high ionic strength, such behaviour does not affect the impact of the nanocrystals on ORR catalysis (vide infra). Moreover, O_2 release experiments confirm that the silicalite-1-NCs reversibly adsorb O_2 at a comparable density as to in the solid state, even when surrounded by an aqueous phosphate electrolyte (Fig. 1D, blue shaded region and Supplementary Table 3).

Impact of silicalite-1-NCs on ORR electrocatalysis. To examine the effect of microporous water on ORR electrocatalysis, we performed rotating disc electrode (RDE) voltammetry on aqueous solutions containing varying concentrations of A-silicalite-1-NCs. ORR by RDE voltammetry enables precise control of convective flow for mass transport[31], where the effects of mass transport and electrode kinetics can be often quantified separately using the Koutecký–Levich equation[32]. A thin film of a commercial carbon-supported platinum catalyst (Pt/C; 60 weight % Pt) on a glassy carbon RDE was employed as the working electrode (Fig. 2A) to be consistent with previously reported ORR studies[27,33–35]; ORR on Pt/C proceeds exclusively via the 4-electron/4-proton reduction pathway[33,34]. A high concentration of phosphate buffer (total phosphorus species of 0.5 M) was employed as the electrolyte solution to maintain the local pH at the cathode near that of the bulk solution.

Fig. 2B shows the recorded current density traces (RDE rotation rate, ω = 1600 rpm) for ORR in phosphate-buffered water at pH 7.0 (black trace) and for increasing concentrations of A-silicalite-1-NCs from 25.0 to 122.7 mg mL^{-1} (Supplementary Table 4). In the absence of A-silicalite-1-NCs, the expected S-shape profile is obtained with a plateau current density of 4.5 mA cm^{-2} as a result of O_2 mass transport limitations; this result is typical of ORR on Pt/C in aqueous solutions where a plateau current density of 4–6 mA cm^{-2} is observed, with the exact value depending on the nature and concentration of the electrolyte[27,34]. Conversely, the plateau current density for ORR increases monotonically with increasing concentration of A-silicalite-1-NCs (Supplementary Fig. 4), attaining a value of 17.5 mA cm^{-2} for phosphate-buffered water containing 122.7 mg mL^{-1} of A-silicalite-1-NCs (Fig. 2B, teal trace). We note that the kinematic viscosity (v; Methods Section, Material characterization) of solutions containing A-silicalite-1-NCs is higher than that of pure phosphate-buffered water (Supplementary Table 6), though the contribution of the kinematic viscosity to the limiting ORR current density (j_{lim}) is minimal owing to a $j_{\text{lim}} \propto v^{-1/6}$ dependence[33].

Fig. 2C shows the increase in the ORR current density with ω for phosphate-buffered water containing A-silicalite-1-NCs at 122.7 mg mL^{-1} (ω dependence for other concentrations of A-silicalite-1-NCs is shown in Supplementary Fig. 5). The increase in ORR current density with rotation rate indicates mass transport limitations, but not exclusively as the observation of a plateau is delayed to lower potentials (i.e.,

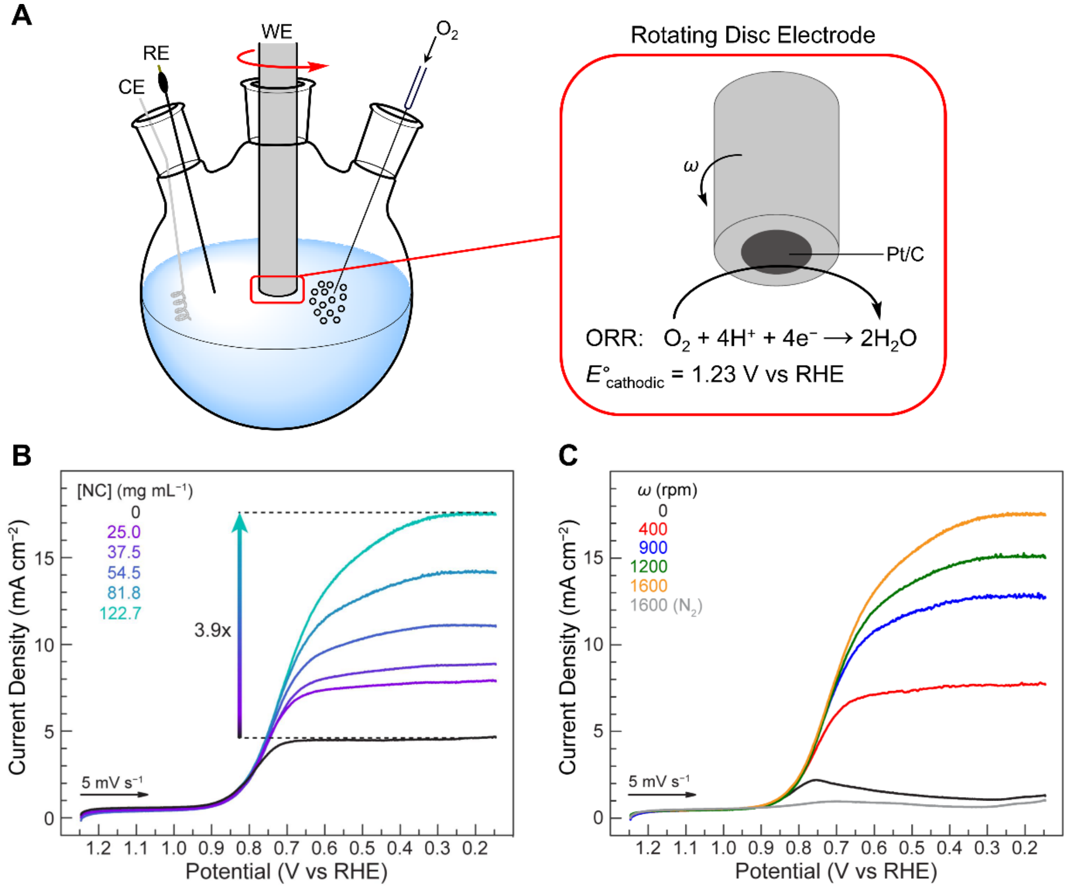

Fig. 2 | ORR catalysis. (**A**) A schematic highlighting the rotating disc electrode (RDE) setup employed for ORR catalysis experiments using a glassy carbon working electrode (WE) with a Pt/C catalyst film, a leakless Ag/AgCl-based reference electrode (RE), and a Pt mesh counter electrode (CE). (**B**) RDE voltammograms collected in O_2-saturated phosphate-buffered water (0.5 M in phosphorus) solutions at pH 7.0 containing 0–122.7 mg mL^{-1} of A-silicalite-1-NCs at a scan rate of 5 mV s^{-1} and an electrode rotation rate of 1600 rpm. (**C**) RDE voltammograms collected in O_2-saturated phosphate-buffered water (0.5 M in phosphorus) solutions at pH 7.0 containing 122.7 mg mL^{-1} of A-silicalite-1-NCs at a scan rate of 5 mV s^{-1} and electrode rotation rates of 0–1600 rpm. The voltammogram collected in N_2-saturated phosphate-buffered water (0.5 M in phosphorus) solution at pH 7.0 at an electrode rotation rate of 1600 rpm is shown in grey for comparison. The reported current density values are normalized by the geometric surface area of the working electrode and all potentials are reported in V vs RHE.

higher overpotentials) as compared to pure phosphate-buffered water. Importantly, the plateau in ORR current density is shifted by over 0.4 V in microporous water (0.7 V vs 0.25 V vs RHE in the absence and presence of A-silicalite-1-NCs, respectively), indicating that the activity-dominated current density of the Pt/C catalyst may be extracted in this potential range (vide infra). The observations of a 3.9× increase in ORR current density together with partially rate limiting catalyst activity for the microporous phosphate electrolyte solutions as compared to pure phosphate-buffered water indicate that hydrophobic silicalite-1-NCs represent a formidable strategy to increase ORR electrocatalytic performance.

Influence of zeolite particle size and type on ORR performance. We next assessed the impact of silicalite-1 particle size on the ORR catalytic performance. As opposed to the cylindrical and larger particle size of A-silicalite-1-NCs, B-silicalite-1-NCs (Methods Section, Material synthesis for synthesis; Supplementary Fig. 6 for PXRD) are spherical (Supplementary Fig. 7) with an average diameter of 92 ± 13 nm (Supplementary Fig. 8 and Supplementary Table 1). The ORR catalysis at selected concentrations (Supplementary Table 7) was examined using the same procedure as for A-silicalite-1-NCs. The overall ORR behaviour is the same for identical concentrations of the two silicalite-1-NC samples (Supplementary Fig. 9), but slightly lower ORR current densities were observed for the smaller particle size, which likely results from their slightly lower O_2 capacity (Supplementary Table 2).

To investigate the impact of the nature of the zeolite nanocrystals on ORR catalytic performance, ORR catalysis on a Pt/C catalyst in phosphate-buffered water (0.5 M in phosphorus) solutions at pH 7.0 was carried out in the presence of aluminosilicate zeolite L nanocrystals (LTL-NCs; Methods Section, Material synthesis for synthesis; Supplementary Fig. 10 for PXRD). LTL-NCs exhibit asymmetric morphology (Supplementary Fig. 11) and feature hydrophilic pores, which are filled with water molecules when immersed in aqueous solution. In contrast to silicalite-1-NCs, LTL-NCs (Supplementary Table 10) do not provide enhanced ORR catalytic current densities for a Pt/C catalyst over that recorded in pure phosphate-buffered water (Supplementary Fig. 12). The poor ORR performance of hydrophilic LTL-NCs is attributed to water-filled pores. As all three types of zeolite-NCs remain intact after ORR operation, as confirmed by PXRD (Fig. 1B and Supplementary Figs. 6 and 10) and SEM (Supplementary Figs. 1, 2, 7, 8, and 11) analyses, these observations indicate that O_2 carried in the dry pores of silicalite-1-NCs in water is critical for increasing the concentration of O_2 in the vicinity of the catalyst and engendering the observed enhancement in ORR current density. As a further support of that explanation, no enhancement in ORR current density is observed in the presence of non-calcined A-silicalite-1-NCs (Supplementary Fig. 17), which feature pores filled with organic structure-directing agent and thus exhibit O_2 capacities similar to that of pure phosphate-buffered water (Supplementary Table 2).

ORR performance in acid. To investigate how the electrolyte impacts ORR catalytic performance of the Pt/C electrocatalyst in the presence of silicalite-1-NCs, we repeated the ORR electrocatalysis study in 0.5 M H_2SO_4 (pH 0.3) solutions containing varying concentrations of A-silicalite-1-NCs from 25.0 to 122.7 mg mL^{-1} (Supplementary Table 17). In the presence of 122.7 mg mL^{-1} of A-silicalite-1-NCs, the ORR current density is 21.1 mA cm^{-2} at 0.25 V vs RHE (ω = 1600 rpm), representing a 3.8× increase over that observed in pure 0.5 M H_2SO_4 solution (Supplementary Figs. 22 and 23). These results are in good agreement with the 3.9× enhancement in ORR current density observed in phosphate-buffered water at pH 7.0, indicating that the presence of silicalite-1-NCs improves ORR catalytic performance so long as the nanocrystals remain stable under the operating conditions of catalysis.

Catalyst stability and particle effects on ORR performance. The Pt/C electrocatalyst in the presence of A-silicalite-1-NCs was investigated to assess whether the Pt/C electrocatalyst in both phosphate-buffered water (pH 7.0) and 0.5 M H_2SO_4 (pH 0.3) solutions is affected by the presence of silicalite-1-NCs. For each electrolyte solution under O_2 saturation, a three-part RDE ORR experiment was performed using a single Pt/C catalyst film. First, the RDE voltammogram was collected in the absence of silicalite-1-NCs, then the RDE voltammogram was collected in the presence of 118.5 mg mL^{-1} of A-silicalite-1-NCs, and finally the RDE voltammogram was collected again in the absence of silicalite-1-NCs. As shown in Supplementary Fig. 26, for both electrolyte solutions, the two RDE voltammograms for the Pt/C electrocatalyst collected pre and post introduction to a 118.5 mg mL^{-1} solution of A-silicalite-1-NCs are identical, indicating that the Pt/C catalyst is not modified in the presence of silicalite-1-NCs.

As suspended particles have been shown to influence mass transport at rotating disc electrodes under certain conditions arising from perturbation of the diffusion layer thickness[36,37], we also investigated whether such particle effects are operative under our experimental conditions. The LTL-NCs offer an ideal control for examining whether nanoparticles affect the observed enhancement in ORR current density as they are of similar chemical composition, morphology, and size to that of A-silicalite-1-NCs. However, as mentioned above, no enhancement in ORR current density is observed for aqueous solutions of LTL-NCs. As a further control, we performed ORR electrocatalytic measurements on identical, but non-calcined A-silicalite-1-NCs. As presented in Supplementary Table 2, non-calcined A-silicalite-1-NCs display minimal porosity due to pore blockage with the immobilized organic structure-directing agents. As shown in Supplementary Figs. 17 and 25, no enhancement in ORR current density is observed for non-calcined A-silicalite-1-NCs in phosphate-buffered water (0.5 M phosphorus, pH 7.0) and 0.5 M H_2SO_4 (pH 0.3) solutions, respectively. Finally, following previously reported approaches to define the influence of suspended particles on mass transfer in RDE experiments, we monitored the ferricyanide to ferrocyanide electroreduction. Supplementary Fig. 27 shows the current density traces for the ferricyanide reduction on a glassy carbon working electrode in Ar-saturated phosphate-buffered water (0.5 M phosphorus, pH 7.0) and 0.5 M H_2SO_4 (pH 0.3) solutions containing varying concentrations of A-silicalite-1-NCs from 25.0 to 122.7 mg mL^{-1}. As displayed in Supplementary Fig. 27, A-silicalite-1-NCs have no significant effects on the RDE voltammograms for ferricyanide reduction in both electrolyte solutions, indicating that changes in diffusion layer thickness arising from inert particle effects are negligible under our operating conditions. These data illustrate that increased O_2 concentration in the vicinity of the electrocatalyst is the primary reason for the observed enhancement in ORR current density in microporous water as opposed to physical perturbation of the electrical double layer.

Electrokinetics modelling of ORR catalysis. Insight into the benefit of microporous water on ORR catalysis is obtained from electrokinetics modelling (Supplementary Note 5) of ORR catalysis in the absence (Supplementary Fig. 28) and presence of silicalite-1-NCs. Fig. 3A shows the electrokinetics model where the bulk O_2-saturated aqueous solution is composed of free O_2 molecules with a diffusion coefficient D_{O_2} in equilibrium with O_2 molecules adsorbed in silicalite-1-NCs (ZO_2) with an apparent diffusion coefficient D_{ZO_2}. As the diffusion coefficient of silicalite-1-NCs (D_z) is ca. 4 orders of magnitude smaller than D_{O_2}, the transport of O_2 by silicalite-1-NCs is best viewed as a hopping-type mechanism of O_2 between nanocrystals in which the equilibrium between O_2 and ZO_2 is fast and such that D_{ZO_2} is of the same order of magnitude as D_{O_2} (Supplementary Fig. 29). The reaction scheme and catalytic sequence employed for the modelling are highlighted in Figs. 3B and 3C, respectively. We note that our model assumes that O_2 molecules adsorbed in silicalite-1-NCs cannot be directly reduced, rather, O_2 needs to desorb prior to reduction, thus giving rise to a CE (chemical step followed by an electrochemical step) type mechanism. The redox characteristics of native catalyst active sites are obtained from fitting the voltammetric features of the catalyst film in the absence of O_2 (Supplementary Fig. 28). This leads to a non-ideal Nernstian behaviour akin to a distribution of standard potentials and blocking of surface sites,

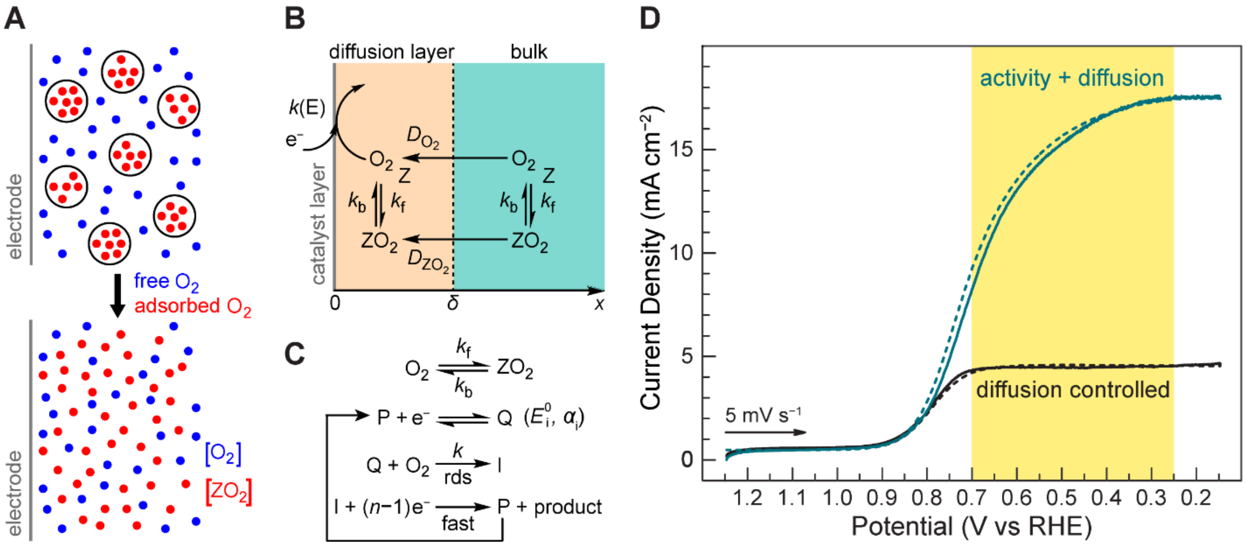

Fig. 3 | Electrokinetics modelling of ORR catalysis. (**A**) Schematic diagram highlighting the foundation of our electrokinetics model for ORR catalysis in the presence of silicalite-1-NCs (here denoted as Z), where the bulk solution is composed of free O_2 molecules (blue spheres) in equilibrium with O_2 molecules adsorbed in silicalite-1-NCs (red spheres). (**B**) Reaction scheme used for electrokinetics modelling. Note that O_2 molecules adsorbed in silicalite-1-NCs (ZO_2) are not able to be directly reduced at the electrode surface, thus leading to a CE type mechanism. (**C**) Summary of the catalytic sequence employed for electrokinetics modelling. P and Q correspond to the oxidized and reduced forms of the active catalyst sites, respectively, I is an intermediate, n is the stoichiometric number (here $n = 4$), $E°$ is the standard reduction potential for the P/Q couple, α is the charge transfer coefficient, k_f, k_b, and k are rate constants, and rds denotes the rate determining step. (**D**) RDE voltammograms collected in O_2-saturated phosphate-buffered water (0.5 M in phosphorus) solutions at pH 7.0 containing 0 (black) and 122.7 (teal) mg mL^{-1} of A-silicalite-1-NCs at a scan rate of 5 mV s^{-1} and an electrode rotation rate of 1600 rpm. The dashed lines correspond to fits to the experimental data (solid lines) using the electrokinetics model highlighted in **A** to **C** and detailed in Supplementary Note 5. The yellow shaded region highlights the expansion of the potential regime in which the activity-dominated current density may be extracted, achieved in the presence of A-silicalite-1-NCs.

which can be rationalized by the polycrystalline nature of Pt/C particles and the possible role of phosphate[38,39] and sulfate[40–42] electrolytes in the redox properties of individual crystal faces of Pt.

The model in Fig. 3 (Supplementary Tables 20 and 21 and Supplementary Tables 22 and 23 summarize parameters in the model for studies in phosphate-buffered water and 0.5 M H_2SO_4 solutions, respectively) furnishes an excellent fit of the experimental data, as shown in Fig. 3D and Supplementary Fig. 30 for studies in phosphate-buffered water (0.5 M in phosphorus, pH 7.0) solutions and in Supplementary Fig. 31 for studies in 0.5 M H_2SO_4 (pH 0.3) solutions. The model predicts maximum kinetic current densities (i.e., in the absence of O_2 mass transport limitations) of 27.4 mA cm^{-2} and 37.6 mA cm^{-2} in phosphate-buffered water and 0.5 M H_2SO_4 solutions, respectively, (Supplementary Fig. 32) whereas the measured ORR plateau current densities in the absence of silicalite-1-NCs are only 4.5 mA cm^{-2} and 5.6 mA cm^{-2} in phosphate-buffered water and 0.5 M H_2SO_4 solutions, respectively. This disparity between calculated and observed current densities highlights the dramatic limitation that O_2 mass transport imposes on the ORR in aqueous media. As shown in Fig. 2B and Supplementary Fig. 22, by employing a solution containing 122.7 mg mL^{-1} (corresponding to 6.7 volume %) of A-silicalite-1-NCs, we observe plateau current densities of 17.5 mA cm^{-2} and 21.4 mA cm^{-2} in phosphate-buffered water and 0.5 M H_2SO_4 solutions, respectively, and thus, are able to approach the calculated achievable current densities. The benefit of employing microporous water for ORR electrocatalysis is further highlighted schematically in Supplementary Fig. 33, in which the O_2 density in non-porous and microporous aqueous electrolyte solutions is compared. Moreover, our strategy enables us to observe the intrinsic catalytic activity of the Pt/C ORR electrocatalyst over a wide potential range. Whereas the apparent catalytic rate constants of $k_{\mathrm{app}} = 2.25 \times 10^{2}$ M^{-1} s^{-1} and $k_{\mathrm{app}} = 3.0 \times 10^{2}$ M^{-1} s^{-1} in phosphate-buffered water and 0.5 M H_2SO_4 solutions, respectively, obtained from the electrokinetics modelling, do not limit ORR in pure electrolyte solutions at applied potentials >0.25 V vs RHE, it is manifested in the curvature of the current density traces extending from 0.7 V to 0.25 V vs RHE (Fig. 3D, yellow shaded region, and Supplementary Fig. 22E). The ability to perform electrocatalysis in such an expanded mixed kinetic- and diffusion-controlled current regime allows a direct experimental measure of the intrinsic activity of catalysts, which should be useful as a tool for the design of new ORR electrocatalysts.

Conclusions

The foregoing results demonstrate the ability of microporous water to improve the ORR catalytic performance of a Pt/C electrocatalyst through increased supply of O_2. A modest concentration of zeolite (6.7 vol %) results in an increase in ORR current by 3.8–3.9× in acidic and neutral electrolyte solutions, exceeding previously examined additives such as concentrated perfluorocarbon (PFC) emulsions (1.8× increase in ORR current with 25 vol % perfluorocarbon emulsions[21]). Beyond lower O_2 capacities, PFCs are very weakly associated, leading to emulsion instability as droplets undergo Ostwald ripening over time, and PFCs are prone to evaporating from the aqueous solution owing to their high vapor pressure. Accordingly, our work highlights a new area of exploration in electrocatalysis centered on the employment of microporous water to achieve highly concentrated solutions of gases at the electrode where catalysis may occur at enhanced current densities and under no or minimal mass transport limitations, thus providing a platform for accessing intrinsic catalytic properties across a wide range of potentials.

Methods

Materials. Sixty (60) weight % platinum on high surface area Ketjenblack EC-300J was used as received from Fuel Cell Store. Anhydrous potassium hydrogen phosphate (98+%) and potassium dihydrogen phosphate (99+%) were used as received from Strem Chemicals. Aluminium hydroxide was used as received from Beantown Chemicals. Tetrapropylammonium hydroxide (ca. 20 weight % in water) was used as received from TCI. Potassium hexacyanoferrate(II) trihydrate (ACS reagent grade, 98.5–102.0%), anhydrous potassium hexacyanoferrate(III) (99.98% trace metals basis), tetraethyl orthosilicate (98%), potassium hydroxide (ACS reagent grade, ≥85%), LUDOX HS-40 colloidal silica (40 weight % SiO_2 in water), HPLC grade ethanol, and Nafion™ perfluorinated resin solution (5 weight % in a mixture of lower aliphatic alcohols and water) were used as received from Sigma Aldrich. Sulfuric acid (TraceMetal™ Grade) was used as received from Fisher Scientific. Nitrogen (99.99%) gas, argon gas (99.99%), and ultra-high purity oxygen (99.994%) gas were used as received from Airgas. All electrolyte solutions were prepared with type I water (EMD Millipore, 18.2 MΩ cm resistivity).

Material synthesis

Synthesis of A-silicalite-1 nanocrystals (A-silicalite-1-NCs). Silicalite-1-NCs exhibiting a cylindrical shape with an average diameter of ca. 200 nm and an average height of ca. 125 nm were synthesized following a procedure adapted from a previous report[30]. In a representative synthesis, aqueous tetrapropylammonium hydroxide (TPAOH, 39.17 mL, 22.3 weight %), type I water (44.52 mL), and tetraethyl orthosilicate (TEOS, 26.31 mL) were combined in a 250-mL glass bottle. The initially biphasic mixture was stirred for 23 h at 500 revolutions per minute (rpm), allowing the TEOS to become hydrolysed in the alkaline environment and liberate ethanol (EtOH) into the solution. Following hydrolysis, the molar ratio of this solution was 9.1 TPAOH : 25 SiO_2 : 880 H_2O : 100 EtOH. The homogenous solution was loaded into a 200-mL Parr acid digestion vessel and the vessel was sealed and heated to 170 °C for 29 h in an oven. After allowing the vessel to cool, the as-synthesized A-silicalite-1-NCs were collected and washed 5 times with type I water in 50-mL centrifuge tubes. Note that 10 min of centrifugation at 7830 rpm (7197 relative centrifugal force, rcf) was sufficient to precipitate the majority of the product. After the final wash, the product was dried in a centrifuge tube at 70 °C. The dried product was collected and finely ground into a powder. This powder was subsequently placed in an enameled crucible and loaded into a tube furnace. The powder was heated in air from room temperature to 550 °C over 2 h and then held at 550 °C for 10 h. After calcination, A-silicalite-1-NCs were allowed to cool and then collected.

Synthesis of B-silicalite-1 nanocrystals (B-silicalite-1-NCs). Silicalite-1-NCs exhibiting a spherical shape with an average diameter of ca. 90 nm were synthesized following a procedure adapted from a previous report[43]. In a representative synthesis, TPAOH (48.88 mL, 22.3 weight %), type I water (13.29 mL) and TEOS (32.83 mL) were combined in a 250-mL glass bottle. The initially biphasic mixture was stirred for 24 h at 500 rpm, allowing the TEOS to become hydrolysed in the alkaline environment and liberate EtOH into the solution. Following hydrolysis, the molar ratio of this solution was 9.1 TPAOH : 25 SiO_2 : 480 H_2O : 100 EtOH. The homogenous solution was loaded into a 200-mL Parr acid digestion vessel and the vessel was sealed and heated to 90 °C for 48 h in an oven. After allowing the vessels to cool, the as-synthesized B-silicalite-1-NCs were collected and washed 6 times with type I water in 50-mL centrifuge tubes. After the final wash, the product was dried in a centrifuge tube at 70 °C. The dried product was collected and finely ground into a powder. This powder was subsequently placed in an enameled crucible and loaded into a tube furnace. The powder was heated in air from room temperature to 550 °C over 30 min and then held at 550 °C for 10 h. After calcination, B-silicalite-1-NCs were allowed to cool and then collected.

Synthesis of zeolite L nanocrystals (LTL-NCs). In a representative synthesis adapted and modified from a previous report[44], potassium hydroxide (KOH; 14.12 g, 0.252 mol) and aluminum hydroxide ($Al(OH)_3$, 2.43 g, 0.0312 mol) were added to type I water (45 mL) in a 100-mL glass jar containing a Teflon-coated stir bar. The resulting solution was heated in an oil bath to 105 °C for about 3 h to allow the $Al(OH)_3$ to dissolve in the alkaline solution. Afterwards, the solution was allowed to cool for 50 min, and subsequently 28.60 mL of 40 weight % LUDOX (14.87 g SiO_2, 0.248 mol SiO_2) was added. The resulting mixture was sonicated briefly before being stirred at room temperature for 20.5 h. Note that over time, the mixture visibly homogenized and completely fluidized. Afterwards, the solution was cooled and loaded into Parr acid digestion vessels. The vessels were sealed and heated to 180 °C in an oven. After allowing the vessels to cool, the as-synthesized LTL-NCs were collected and diluted with type I water and precipitated via centrifugation at 7830 rpm (7197 rcf). The supernatant was then removed, and fresh type I water was added to the centrifuge tubes. The centrifugation process was repeated for a total of 15 cycles to give a crude aqueous solution of LTL-NCs.

Synthesis of non-calcined A-silicalite-1 nanocrystals (non-calcined A-silicalite-1-NCs). The synthetic procedure was adapted from the same report used to make calcined A-silicalite-1-NCs[30]. In a representative synthesis, aqueous TPAOH (33.27 mL, 22.7 weight %), type I water (39.74 mL), and TEOS (22.99 mL) were combined in a 250-mL glass bottle. The initially biphasic mixture was stirred for 24 h at 500 rpm, allowing the TEOS to become hydrolysed in the alkaline environment and liberate EtOH into the solution. Following hydrolysis, the molar ratio of this solution was 9.1 TPAOH : 25 SiO_2 : 880 H_2O : 100 EtOH. The homogenous solution was loaded into a 200-mL Parr acid digestion vessel and the vessel was sealed and heated to 170 °C for 31 h in an oven. After allowing the vessel to cool, the as-synthesized A-silicalite-1-NCs were collected and washed extensively with type I water to remove excess structure-directing agent (SDA). Note that the SDA is partitioned between the interior and exterior of the nanocrystals; the former cannot be removed by simple washing with water as the pore apertures are too narrow to permit SDA migration. Thus, washing with water was aimed at removing all accessible SDA and uncrystallized SiO_2 from the reaction solution. Washing was assumed to be complete when no further change was observed in the residual organic content of the sample, assessed as follows. After 7 washes with type I water in 50-mL centrifuge tubes, an aliquot was taken and dried for thermogravimetric analysis (TGA) to quantify the residual non-SiO_2 content, which was found to be 13%. The sample was subsequently washed 5 more times, and a new aliquot was taken for TGA analysis. Since the residual non-SiO_2 content of this sample remained about the same, the sample was assumed to be fully washed, and the remaining non-SiO_2 content was assumed to be mostly SDA that was trapped inside the pores of the zeolite. Upon completion of the washing step, the sample was recombined into a single tube and diluted with sufficient type I water to obtain a fluid solution with relatively low viscosity that was used directly for analysis.

Formation of aqueous solutions of activated silicalite-1-NCs. To create a solution of activated A-silicalite-1-NCs, a calcined powder consisting of A-silicalite-1-NCs was added to type I water and sonicated in an ultrasonic bath at 40 kHz frequency for 40 h. To purify and remove large aggregates suspended in solution, the aqueous dispersion was centrifuged at 1500 rpm (264 rcf) for 15 min. After transferring the supernatant to a new centrifuge tube, the dispersion was then centrifuged 3 more times at 1500 rpm for 5 min each, and the supernatant was decanted into a new tube each time. After the last centrifugation cycle, A-silicalite-1-NCs were washed once by centrifuging at 7830 rpm (7197 rcf) for 15 min, discarding the supernatant, and redispersing the precipitated A-silicalite-1-NCs in fresh type I water. The preparation of aqueous solutions of activated B-silicalite-1-NCs was performed in a similar manner as the procedure detailed for A-silicalite-1-NCs, with slight modifications to the duration of sonication and specific purification steps.

Formation of aqueous solutions of LTL-NCs. After completion of 15 washes, the crude LTL-NCs were dispersed in 35 mL of type I water. To purify and remove large aggregates, this solution was subjected to size selection by centrifugation at 7830 rpm (7197 rcf) for variable time periods ranging between 1 and 5 min, with the resulting precipitate inspected for visible white aggregates. The supernatant was decanted into a fresh tube each time and the size selection process was continued until very little white precipitate was observed.

Catalyst film preparation. A catalyst ink was prepared by mixing 5 mg of 60 weight % platinum on high surface area Ketjenblack EC-300J with 990 μL of EtOH and 10 μL of Nafion^{TM} perfluorinated resin solution (5 weight % in a mixture of lower aliphatic alcohols and water). The ink was sonicated for at least 30 min to provide a homogeneous dispersion and 10 μL of this dispersion were dropcasted onto a 5 mm diameter (0.196 cm^2 geometric surface area) glassy carbon rotating disc electrode (Pine Research). Prior to use, the glassy carbon electrode was polished using 0.3 μm Alpha alumina powder (CH Instruments) and rinsed with a copious amount of type I water and EtOH, then subsequently dried in air. Note that the resulting black film contained approximately 0.03 mg of platinum. The film was dried in air and wetted with a minimum amount of type I water before being immersed in the sample solution. The average thickness of the catalyst film was estimated to be on the order of a few μm (<5 μm) using a Tyler Hobson Coherence Correlation Interferometry (CCI) high resolution 3D non-contact optical profiler.

Material characterization

General characterization methods. pH measurements were carried out using a Thermo Scientific Orion^{TM} 9107APMD double-junction pH electrode with automatic temperature compensation, connected to a VWR sympHony SP70P pH meter. The pH electrode was calibrated using standardized pH buffer solutions at 4.01, 7.00, and 10.01 (Thermo Scientific Orion^{TM}).

Powder X-ray diffraction (PXRD) data were collected at ambient temperature on a D2 Phaser Bruker AXS diffractometer with CuK_α radiation (λ = 1.5418 Å). Each sample was dried and placed onto a low-background Si wafer for measurement. The PXRD data collected for zeolite nanocrystals (zeolite-NCs) before and after performing oxygen reduction reaction (ORR) catalysis are provided in Fig. 1B and Supplementary Fig. 18 (A-silicalite-1-NCs), Supplementary Fig. 6 (B-silicalite-1-NCs), Supplementary Fig. 10 (LTL-NCs), and Supplementary Figs. 13 and 24 (non-calcined A-silicalite-1-NCs).

BET analysis was used to determine surface areas for the zeolite-NCs from N_2 adsorption isotherms collected at 77 K. For 77 K N_2 surface area measurements, gas adsorption for solid samples was measured at a minimum of 50 different pressures between 0 and 0.9 bar, with at least 45 points collected below 0.1 bar (Supplementary Note 1).

Nanocrystal size analysis. Field emission scanning electron microscopy (SEM) and dynamic light scattering (DLS) were used to quantify the size distribution of the synthesized nanocrystals. SEM analysis of zeolite-NCs was performed using a Zeiss Ultra Plus instrument. The SEM was operated at an electron beam voltage of 20 kV at a working distance of 5.0 mm and an in-lens secondary electron detector was used for imaging. In a representative measurement, Si wafers sample holders were washed by sonicating with acetone and isopropanol before being loaded into a plasma cleaner. To prepare samples for imaging, aqueous zeolite-NC solutions were diluted with EtOH and this ethanolic solution was dropcasted onto the Si substrate. All samples were sputter coated with a 5-nm or 10-nm layer of 80:20 Pt:Pd. To calculate the size distributions of calcined and non-calcined A-silicalite-1-NCs and B-silicalite-1-NCs, SEM images were analysed using ImageJ. Each size distribution was computed using at least 100 individual silicalite-1-NCs. Note that the reported size of a single silicalite-1-NC was defined and calculated as the equivalent diameter of a circle having the same area as each silicalite-1-NC. For A-silicalite-1-NCs, the size was defined in the top-down direction. No significant size changes were observed after ORR catalysis in both 0.5 M potassium phosphate (KP_i) and 0.5 M H_2SO_4 solutions, regardless of whether the silicalite-1-NCs were calcined or not. In all cases, the mean diameter was within one standard deviation between samples measured before and after ORR catalysis. These data are presented graphically in Supplementary Figs. 2 and 20 (calcined A-silicalite-1-NCs), Supplementary Fig. 8 (B-silicalite-1-NCs), and Supplementary Fig. 15 (non-calcined A-silicalite-1-NCs), and summarized in Supplementary Tables 1 and 16.

DLS analysis was used to determine the size distributions of silicalite-1-NCs in aqueous solutions. DLS measurements were performed using a Malvern Panalytical Zetasizer Ultra instrument. To prepare samples for measurements, aqueous silicalite-1-NC solutions were diluted with type I water, 0.5–1.0 M KP_i buffer (pH 7.0), or 0.5–1.0 M H_2SO_4 to give a final concentration of ca. 1 mg mL^{-1} of silicalite-1-NCs in type I water with and without 0.5 M KP_i buffer (pH 7.0) or 0.5 M H_2SO_4 electrolyte. Note that dilution is required to obtain accurate DLS data. Samples were sonicated or vortexed for at least 10 s right before data acquisition. The reported data are an average of 5–6 individual measurements on a representative silicalite-1-NC sample, where each measurement is an average of at least 5 runs. The data are reported as intensity distribution in lieu of number distribution owing to the non-applicability of certain criteria needed to transform the former into the latter. Mie theory, used to convert intensity distribution to number distribution,[45] is only accurate when the solution is homogeneous and spherically symmetric, and both the real and imaginary components of the refractive index of the solution must be known. The obtained particle size distribution curves for calcined A-silicalite-1-NCs in aqueous solutions are shown in Fig. 1C and Supplementary Figs. 3 and 21, and the analogous size distribution curves obtained for non-calcined A-silicalite-1-NCs are provided in Supplementary Fig. 16. The particle size distribution curves for B-silicalite-1-NCs in neutral aqueous solutions are given in Supplementary Fig. 3. We note that A-silicalite-1-NCs do undergo aggregation over time in aqueous solutions of high ionic strength, and this is especially pronounced in strongly acidic electrolyte solutions (e.g., 0.5 M H_2SO_4); however, such aggregation does not affect the impact of A-silicalite-1-NCs on ORR catalysis with Pt/C electrocatalyst in aqueous solutions (vide supra).

Solid-state gas adsorption measurements. Gas adsorption measurements were carried out on solid zeolite-NCs at 77 K for N_2 and at 20 °C for O_2. Samples for measurements were activated prior to measurement by heating to 175 °C and evacuating using a Smart VacPrep gas adsorption sample preparation device (Micromeritics Instrument Corp.) equipped with a turbomolecular pump. Sample analysis was performed using a Micromeritics MicroActive 3Flex 3500 adsorption analyser. To maintain a constant temperature during measurements and minimize fluctuations during O_2 isotherm measurements, the sample analysis tubes were immersed in a large, jacketed water bath that was held at 20 °C (temperature error of approximately ± 0.4 °C). O_2 isotherms were collected by measuring gas adsorption at 20 different pressures in roughly 0.05 bar increments between 0 and 1 bar. The O_2 Henry's constants of solid zeolite-NCs were obtained from the slope of the linear fit applied to the obtained data (Supplementary Table 2).

Bulk O_2 concentration measurements. Measurements of the bulk concentration of dissolved O_2 were carried out concurrently with electrochemical analysis using a PyroScience GmbH FireSting-PRO optical O_2 meter equipped with a temperature sensor for automatic temperature compensation. A self-adhesive O_2 sensor spot was attached to the interior and exterior of the glass vessel used as a sample holder for electrochemical measurements. The sensor was calibrated against freshwater conditions using a two-point calibration employing the factory calibration value for 0% O_2 and the measured value of air-saturated type I water as the two calibration points. The readouts from the O_2 sensor were used to estimate when saturation conditions under specific gas environments were reached. Note that the readouts from the O_2 sensor were corrected to account for the salinity of the 0.5 M KP_i buffer (pH 7.0) solution (conversion factor of 0.710, see Supplementary Note 2). During all electrochemical measurements in N_2-saturated buffer solutions, the bulk concentration of dissolved O_2 was lower than 50 μM. During all electrochemical measurements in O_2-saturated buffer solutions, the bulk concentration of dissolved O_2 was 1.0(1) mM (Supplementary Note 2). Note that the dissolved O_2 content could not be monitored in situ during electrochemical analysis in 0.5 M H_2SO_4 solutions due to incompatibility of the sensor with strongly acidic environments, thus identical gas purge times as in 0.5 M KP_i buffer solutions were used.

Oxygen capacity of aqueous zeolite-NC solutions. The experimental O_2 capacity of A-silicalite-1-NC electrolyte solutions was determined from O_2 release measurements in deoxygenated type I water using a Clark electrochemical O_2 sensor (Unisense MicroRespiration O_2 microsensor). The details of the measurements and associated calculations are provided in Supplementary Note 3.

Viscosity measurements. Dynamic viscosity measurements of 0.5 M KP_i buffer and 0.5 M H_2SO_4 sample solutions with and without zeolite-NCs were conducted at 20 °C using a Kyoto Electronics Manufacturing Co., Ltd. electromagnetically spinning sphere viscometer (model EMS-1000S) equipped with a temperature-controlled sample holder[46]. Samples were loaded into a glass sample tube equipped with an aluminium ball probe of either 2.0-mm (0.5 M KP_i and 0.5 M H_2SO_4 sample solutions with and without calcined or non-calcined A-silicalite-1-NCs or B-silicalite-1-NCs) or 4.7-mm diameter (0.5 M KP_i and 0.5 M H_2SO_4 sample solutions with and without LTL-NCs), and enough sample was added such that the height of the sample in the tube was at least 3 times the diameter of the ball used (a requisite condition of the physical model employed by the viscometer). Specifically, at least 400 and 800 μL of sample were used when the 2.0-mm and 4.7-mm aluminium balls were employed, respectively. The aluminium ball was rotated at a rate of 500–1000 Hz and its movement was traced with a red laser. The viscosity of each sample was determined by the reduction in the rotation rate of the aluminium ball. Measurements using the 2.0-mm and 4.7-mm aluminium balls were conducted with measuring times of 1 s and 5 s, respectively. All measurements on zeolite-NC samples were conducted after ultrasonication at 37 kHz for 30 min or vigorous vortexing for at least 10 s. To ensure that temperature equilibration was achieved, the reported data are an average of at least 5 individual measurements recorded after leaving the sample in the viscometer for at least 10 min. The dynamic viscosity data obtained for sample solutions of A-silicalite-1-NCs, B-silicalite-1-NCs, LTL-NCs, and non-calcined A-silicalite-1-NCs are provided in Supplementary Tables 5 and 18, 8, 11, and 14, respectively. Note that the dynamic viscosity values for non-calcined A-silicalite-1-NCs in 0.5 M KP_i and 0.5 M H_2SO_4 solutions and calcined A-silicalite-1-NCs in 0.5 M H_2SO_4 solutions increased over time, likely due to settling of the particles, thus the reported values may be an underestimation of the dynamic viscosity of the sample solutions during ORR catalysis.

Kinematic viscosity values (in $mm^2\ s^{-1}$) of the sample solutions were obtained from the measured dynamic viscosity values (in mPa·s) by dividing the dynamic viscosity values by the density of the sample solutions. The error bars for the kinematic viscosity values were determined by error propagation. Note that density values for the zeolite-NC sample solutions were calculated using Supplementary Equation 24 (silicalite-1-NCs) and Supplementary Equation 25 (LTL-NCs), as described in Supplementary Note 4. The density of 0.5 M KP_i (pH 7.0) buffer and 0.5 M

H_2SO_4 (pH 0.3) solutions in the absence of zeolite-NCs was measured to be 1.050 g mL^{-1} (1050 g L^{-1}) and 1.010 g mL^{-1} (1010 g L^{-1}), respectively. Supplementary Tables 4 and 17 (A-silicalite-1-NCs), 7 (B-silicalite-1-NCs), 10 (LTL-NCs), and 13 (non-calcined A-silicalite-1-NCs) list the calculated zeolite-NC sample solution densities. The kinematic viscosity data are provided in Supplementary Tables 6 and 19, 9, 12, and 15 for A-silicalite-1-NCs, B-silicalite-1-NCs, LTL-NCs, and non-calcined A-silicalite-1-NCs, respectively.

Electrochemical procedures

General descriptions. Electrochemical experiments were conducted in a three-electrode electrochemical cell (working, reference, and counter electrodes) at ambient temperature on a CH Instruments potentiostat/galvanostat (model 760D) using a leak-free Ag/AgCl-based reference electrode (LF-1 from Warner Instruments) and a counter electrode comprised of a platinum mesh (99.9%, 52 mesh woven from 0.1 mm diameter wire, Alfa Aesar) attached to a platinum wire (99.95%, 0.5 mm diameter, Alfa Aesar). Prior to use, platinum counter electrodes were cleaned by soaking in concentrated nitric acid (TraceSELECT^{TM}, Fisher Scientific) followed by drying with a butane flame. The leak-free Ag/AgCl-based reference electrode was calibrated using the redox potential of potassium ferri/ferrocyanide in 0.5 M KP_i buffer solution at pH 7.0[47].

Electrode potentials (E) were converted to the reversible hydrogen electrode (RHE) scale using the following relation:

$$E_{\mathrm{RHE}} = E_{\mathrm{Ag/AgCl}} + 0.05836\ \mathrm{V} \times \mathrm{pH} \qquad (1)$$

where E_{RHE} is the converted potential vs RHE and $E_{\mathrm{Ag/AgCl}}$ is the experimentally measured potential vs a leak-free Ag/AgCl-based reference electrode that has been calibrated to the ferri/ferrocyanide redox couple. Note that a solution temperature of 21 °C (294.15 K) and a pH value of 7.0 (0.5 M KP_i) or 0.3 (0.5 M H_2SO_4) were employed for determining E_{RHE} for all experiments. Negative currents correspond to anodic reactions (oxidation) and positive currents correspond to cathodic reactions (reduction).

Rotating disk electrode voltammetry. Rotating disc electrode (RDE) voltammetry experiments were carried out for samples with and without zeolite-NCs at variable electrode rotation rates (0, 400, 900, 1200, 1600 rpm) in 0.5 M KP_i buffer (pH 7.0) or 0.5 M H_2SO_4 (pH 0.3) solutions under both N_2 and O_2 saturation conditions. Specifically, each sample solution was first saturated with nitrogen gas (bulk concentration of dissolved O_2 below 50 μM) and the working electrode was preconditioned by scanning anodically from the open circuit potential in the potential range of −0.05 to 1.45 V vs RHE (0.5 M KP_i, pH 7.0) or −0.04 to 1.36 V vs RHE (0.5 M H_2SO_4, pH 0.3) at a scan rate of 50 mV s^{-1} and an electrode rotation rate of 0 rpm for 10 cycles. Then, a single cyclic voltammetry (CV) scan was collected in the potential range of 0.15 to 1.25 V vs RHE by scanning anodically from 0.95 V vs RHE at a scan rate of 5 mV s^{-1} and an electrode rotation rate of 1600 rpm. Afterwards, the sample solution was saturated with oxygen gas (bulk concentration of dissolved O_2 of 1.0(1) mM and 1.3(1) mM in 0.5 M KP_i buffer and 0.5 M H_2SO_4 solutions, respectively). Note that the working electrode was not immersed in the sample solution during the gas saturation processes but kept wetted with type I water to avoid delamination. Single CV scans were collected for the O_2-saturated sample solutions in the potential range of 0.15 to 1.25 V vs RHE by scanning anodically from 0.95 V vs RHE at a scan rate of 5 mV s^{-1} and variable electrode rotation rates of 0 to 1600 rpm. To investigate the influence of suspended silicalite-1-NCs on the mass transfer at a rotating disc electrode, the reduction of $K_3[Fe(CN)_6]$ was analyzed in 0.5 M KP_i buffer or 0.5 M H_2SO_4 solutions containing varying amounts of A-silicalite-1-NCs under Ar saturation conditions using a glassy carbon working electrode. These data are provided in Supplementary Fig. 27. All RDE voltammetry experiments were conducted with a continuous gas flow into the sample solution at a rate of

$1.7(2) \times 10^{2}$ mL min^{-1}, controlled using a mass flow controller (MKS Technology Inc.). Uncompensated solution resistance (R_u) was determined to be 1.5–3.7 Ω (0.5 M $\mathrm{KP_i}$, pH 7.0) and 0.2–0.9 Ω (0.5 M H_2SO_4, pH 0.3) using the potential step method (50 mV amplitude) around the open circuit potential. Note, however, that all potentials are reported without applying iR_u compensation and any background correction. A baseline correction was applied to aid in the comparison of RDE voltammetry data collected for 0.5 M $\mathrm{KP_i}$ buffer solutions at pH 7.0 in the absence and presence of non-calcined A-silicalite-1-NCs. Specifically, the data collected in the presence of non-calcined A-silicalite-1-NCs was adjusted so that the current density at 1.1 V vs RHE was equivalent for all three data sets displayed in Supplementary Fig. 17C. All current densities are reported based on the geometric electrode surface area (0.196 cm^2). Independently prepared samples of each type were measured to ensure reproducibility. The provided data are representative examples.

Electrokinetics modelling. RDE voltammograms collected for samples with and without A-silicalite-1-NCs at variable electrode rotation rates in 0.5 M $\mathrm{KP_i}$ buffer and 0.5 M H_2SO_4 solutions under N_2 and O_2 saturation conditions were simulated using analytical equations derived according to the reaction scheme and catalytic sequence displayed in Figs. 3B and 3C. The details of electrokinetics modelling and associated equations are provided in Supplementary Note 5.

Data availability

The data that support the findings of this study are presented in the article and Supplementary Information. All data are available from the authors upon reasonable request.

Acknowledgments

This work was supported by a Multidisciplinary University Research Initiative, sponsored by the U.S. Department of the Navy, Office of Naval Research, under grant no. N00014-20-1-2418 (D.G.N., J.A.M.), Star-Friedman Challenge grant from Harvard University (D.G.N., J.A.M.), and Labex ARCANE, CBμH-EUR-GS, and ANR-17-EURE-0003 from the Agence Nationale de la Recherche (C.C.). J.A.M. acknowledges support from the Arnold and Mabel Beckman Foundation through a Beckman Young Investigator Grant. Part of this work was performed at the Center for Nanoscale Systems (CNS), a member of the National Nanotechnology Coordinated Infrastructure Network (NNCI), which is supported by the National Science Foundation under NSF award no. 1541959. A.E.T. acknowledges the Harvard University Center for the Environment for a postdoctoral fellowship, and D.P.E. acknowledges support from a DoD National Defense Science and Engineering (NDSEG) fellowship. We thank B. Johnston, J. Cho, and J. Shen for experimental assistance and Drs. M. I. Gonzalez, M. J. Nava, J. Ryu, and Z. Yan for helpful discussions. We would also like to thank Prof. G. M. Whitesides and Dr. M. S. Kodaimati for lending us a mass flow controller for the electrochemical experiments.

Author contributions

A.E.T., D.P.E., D.G.N., and J.A.M. conceived the project. D.P.E. and J.A.M. designed the zeolite materials, and D.P.E. carried out the synthesis. A.E.T., D.G.N., C.C., and J.A.M. designed electrochemical experiments, and A.E.T. performed the electrochemical experiments. A.E.T. and D.P.E. performed testing and characterizations. C.C. performed electrokinetics modelling. All authors contributed to the manuscript preparation.

Competing interests

D.P.E. and J.A.M. are inventors on a patent application related to O_2 concentration in microporous aqueous solutions held and submitted by Harvard University.

Additional information

Supplementary information. The online version contains supplementary material available at XXX.
Correspondence and requests for materials should be addressed to C. Costentin, J. A. Mason, or D. G. Nocera.

References

1. Nocera, D. G. Proton-coupled electron transfer: The engine of energy conversion and storage. *J. Am. Chem. Soc.* **144**, 1069–1081 (2022).
2. Stančin, H., Mikulčić, H., Wang, X. & Duić, N. A review on alternative fuels in future energy system. *Renew. Sustain. Energy Rev*. **128**, 109927 (2020).
3. Weber, R. S. Effective use of renewable electricity for making renewable fuels and chemicals. *ACS Catal.* **9**, 946‒950 (2019).
4 Nocera, D. G. Solar fuels and solar chemicals industry. *Acc. Chem. Res.* **50**, 616–619 (2017).
5. Lewis, N. S. & Nocera, D. G. Powering the planet: Chemical challenges in solar energy utilization. *Proc. Natl. Acad. Sci. U.S.A.* **103**, 15729–15735 (2006).
6. Cook, T. R., Dogutan, D. K., Reece, S. Y., Surendranath, Y., Teets, T. S. & Nocera, D. G. Solar energy supply and storage for the legacy and nonlegacy worlds. *Chem. Rev*. **110**, 6474–6502 (2010).
7. Spitler, M. T., Modestino, M. A., Deutsch, T. G., Xiang, C. X., Durrant, J. R., Esposito, D. V., Haussener, S., Maldonado, S., Sharp, I. D., Parkinson, B. A., Ginley, D. S., Houle, F. A., Hannappel, T., Neale, N. R., Nocera, D. G. & McIntyre, P. C. Practical challenges in the development of photoelectrochemical solar fuels production. *Sustain. Energy Fuels* **4**, 985–995 (2020).
8. Staffell, I., Scamman, D., Velazquez Abad, A., Balcombe, P., Dodds, P. E., Ekins, P., Shah, N. & Ward, K. R. The role of hydrogen and fuel cells in the global energy system. *Energy Environ. Sci.* **12**, 463–491 (2019).
9. Battino, R., Seybold, P. G. & Campanell, F. C. Correlations involving the solubility of gases in water at 298.15 K and 101325 Pa. *J. Chem. Eng. Data* **56**, 727–732 (2011).
10. Higgins, D., Hahn, C., Xiang, C., Jaramillo, T. F. & Weber, A. Z. Gas-diffusion electrodes for carbon dioxide reduction: A new paradigm. *ACS. Energy Lett*. **4**, 317–324 (2019).
11. Rabiee, H., Ge, L., Zhang, X., Hu, S., Li, M. & Yuan, Z. Gas diffusion electrodes (GDEs) for electrochemical reduction of carbon dioxide, carbon monoxide, and dinitrogen to value-added products: A review. *Energy Environ. Sci*. **14**, 1959–2008 (2021).
12. Lees, E. W., Mowbray, B. A. W., Parlane, F. G. L. & Berlinguette, C. P. Gas diffusion electrodes and membranes for CO_2 reduction electrolysers. *Nat. Rev. Mater*. **7**, 55–64 (2022).
13. Wakerley, D., Lamaison, S., Wicks, J., Clemens, A., Feaster, J., Corral, D., Jaffer, S. A., Sarkar, A., Fontecave, M., Duoss, E. B., Baker, S., Sargent, E. H., Jaramillo, T. F. & Hahn, C. Gas diffusion electrodes, reactor designs and key metrics of low-temperature CO_2 electrolysers. *Nat. Energy* **7**, 130–143 (2022).
14. Nesbitt, N. T., Burdyny, T., Simonson, H., Salvatore, D., Bohra, D., Kas, R. & Smith, W. A. Liquid–solid boundaries dominate activity of CO_2 reduction on gas-diffusion electrodes. *ACS Catal*. **10**, 14093–14106 (2020).
15. Yang, K., Kas, R., Smith, W. A. & Burdyny, T. Role of the carbon-based gas diffusion layer on flooding in a gas diffusion electrode cell for electrochemical CO_2 reduction. *ACS Energy Lett*. **6**, 33–40 (2021).
16. Tan, Y. C., Quek, W. K., Kim, B., Sugiarto, S., Oh, J. & Kai, D. Pitfalls and protocols: Evaluating catalysts for CO_2 reduction in electrolyzers based on gas diffusion electrodes. *ACS Energy Lett*. **7**, 2012–2023 (2022).
17. Hone, C. A. & Kappe, C. O. Membrane microreactors for the on-demand generation, separation, and reaction of gases. *Chem. Eur. J*. **26**, 13108–13117 (2020).
18. Luo, T., Abdu, S. & Wessling, M. Selectivity of ion exchange membranes: A review. *J. Membr. Sci.* **555**, 429–454 (2018).
19. Oener, S. Z., Foster, M. J. & Boettcher, S. W. Accelerating water dissociation in bipolar membranes and for electrocatalysis. *Science* **369**, 1099–1103 (2020).
20. Sato, T., Hamada, Y., Sumikawa, M., Araki, S. & Yamamoto, H. Solubility of oxygen in organic solvents and calculations of the Hansen solubility parameters of oxygen. *Ind. Eng. Chem. Rev*. **53**, 19331–19337 (2014).
21. Kronberger, H., Bruckner, K. & Fabjun, C. Reduction of oxygen from electrolyte emulsions with high oxygen contents. *J. Power Sources* **86**, 562–567 (2000).

22. O’Reilly, N., Giri, N. & James, S. L. Porous liquids. *Chem. Eur. J*. **13**, 3020–3025 (2007).
23. Giri, N., Del Pópolo, M. G., Melaugh, G., Greenaway, R. L., Rätzke, K., Koschine, T., Pison, L., Costa Gomes, M. F., Cooper, A. I. & James, S. L. Liquids with permanent porosity. *Nature* **527**, 216–220 (2015).
24. Fulvio, P. F. & Dai, S. Porous liquids: The next frontier. *Chem* **6**, 3263–3287 (2020).
25. Bavykina, A., Cadiau, A. & Gascon, J. Porous liquids based on porous cages, metal organic frameworks and metal organic polyhedra. *Coord. Chem. Rev.* **386**, 85–95 (2019).
26. Erdosy, D. P., Wenny, M. B., Cho, J., DelRe, C., Walter, M. V., Jimenez-Ángeles, F., Qiao, B., Sanchez, R., Peng, Y., Polizzotti, B. D., Olvera de la Cruz, M. & Mason, J. A. Microporous water with high gas solubilities. *Nature*, **608**, 712–718 (2022).
27. Wang, X., Li, Z., Qu, Y., Yuan, T., Wang, W., Wu, Y. & Li, Y. Review of metal catalysts for oxygen reduction reaction: From nanoscale engineering to atomic design. *Chem* **5**, 1486–1511 (2019).
28. Flanigen, E. M., Bennett, J. M., Grose, R. W., Cohen, J. P., Patton, R. L., Kirchner, R. M. & Smith, J. V. Silicalite, a new hydrophobic crystalline silica molecular sieve. *Nature* **271**, 512–516 (1978).
29. Díaz, I., Kokkoli, E., Terasaki, O. & Tsapatsis, M. Surface structure of zeolite (MFI) crystals. *Chem. Mater*. **16**, 5226–5232 (2004).
30. Butt, T. & Tosheva, L. Synthesis of colloidal silicalite-1 at high temperatures. *Microporous Mesoporous Mater.* **187**, 71–76 (2014).
31. Lazaridis, T., Stühmeier, B. M., Gasteiger, H. A. & El-Sayed, H. A. Capabilities and limitations of rotating disk electrodes versus membrane electrode assemblies in the investigations of electrocatalysts. *Nat. Catal*. **5**, 363–373 (2022).
32. Bard, A. J. & Faulkner, L. R. *Electrochemical Methods: Fundamentals and Applications* (Wiley, New York, 2000).
33. Zhong, G., Xu, S., Liu, L., Zheng, C. Z., Dou, J., Wang, F., Fu, X., Liao, W. & Wang, H. Effect of experimental operations on the limiting current density of oxygen reduction reaction evaluated by rotating-disk electrode. *ChemElectroChem* **7**, 1107–1114 (2020).
34. Paulus, U. A., Schmidt, T. J., Gasteiger, H. A. & Behm, R. J. Oxygen reduction on a high-surface area Pt/Vulcan carbon catalyst: A thin-film rotating ring-disc electrode study. *J. Electroanal. Chem*. **495**, 134–145 (2001).
35. You, B., Jiang, N., Sheng, M., Drisdell, W. S., Yano, J. & Sun, Y. Bimetal–organic framework self-adjusted synthesis of support-free nonprecious electrocatalyst for efficient oxygen reduction. *ACS Catal*. **5**, 7068–7076 (2015).
36. De Ficquelmont-Loizos, M. M., Tamisier, L. & Caprani, A. Mass transfer in laminar flow at a rotating disc electrode in suspensions of inert particles. *J. Electrochem. Soc*. **135**, 626–634 (1988).
37. Sonneveld, P. J., Visscher, W. & Barendrecht, E. The influence of suspended particles on the mass transfer at a rotating disc electrode. Non-conducting particles. *J. Appl. Electrochem*. **20**, 563–574 (1990).
38. He, Q., Yang, X., Chen, W., Mukerjee, S. & Koel, B. Influence of phosphate anion adsorption on the kinetics of oxygen electroreduction on low index Pt(*hkl*) single crystals. *Phys. Chem. Chem. Phys*. **12**, 12544–12555 (2010).
39. Gómez-Marín, A. M. & Feliu, J. M. “Oxygen reduction on platinum single crystal electrodes” in *Encyclopedia of Interfacial Chemistry: Surface Science and Electrochemistry* 820–830 (Elsevier, Amsterdam, 2018).
40. Marković, N. M., Gasteiger, H. A. & Ross, Jr., P. N. Oxygen reduction on platinum low-index single-crystal surfaces in sulfuric acid solution: Rotating ring—Pt(*hkl*) disc studies. *J. Phys. Chem*. **99**, 3411–3415 (1995).
41. Wang, J. X., Markovic, N. M. & Adzic, R. R. Kinetic analysis of oxygen reduction on Pt(111) in acid solutions: Intrinsic kinetic parameters and anion adsorption effects. *J. Phys. Chem. B* **108**, 4127–4133 (2004).
42. Nishikawa, H., Yano, H., Inukai, J., Tryk, D. A., Iiyama, A. & Uchida, H. Effects of sulfate on the oxygen reduction reaction activity on stabilized Pt skin/PtCo alloy catalysts from 30 to 80 °C. *Langmuir* **34**, 13558–13564 (2018).

43. Persson, A. E., Schoeman, B. J., Sterte, J. & Otterstedt, J.-E. The synthesis of discrete colloidal particles of TPA-silicalite-1. *Zeolites* **14**, 557–567 (1994).

44. Tsapatsis, M., Lovallo, M., Okubo, T., Davis, M. E. & Sadakata, M. Characterization of zeolite L nanoclusters. *Chem. Mater.* **7**, 1734–1741 (1995).

45. Nobbmann, U. & Morfesis, A. Light scattering and nanoparticles. *Mater. Today* **12**, 52–54 (2009).

46. Sakai, K., Hirano, T. & Hosoda, M. Electromagnetically spinning sphere viscometer. *Appl. Phys. Express* **3**, 016602 (2010).

47. O'Reilly, J. E. Oxidation–reduction potential of the ferro–ferricyanide system in buffer solutions. *Biochim. Biophys. Acta* **292**, 509–515 (1973).